

Near-Infrared Spectroscopy of the Cassiopeia A and Kepler Supernova Remnants

Christopher L. Gerardy and Robert A. Fesen

*6127 Wilder Laboratory, Department of Physics & Astronomy,
Dartmouth College, Hanover, NH 03755-3528*

ABSTRACT

Near-infrared spectra ($0.95 - 2.4 \mu\text{m}$) of the Cassiopeia A and Kepler supernova remnants (SNRs) are presented. Low-dispersion ($R \approx 700$) spectra were obtained for five bright fast-moving ejecta knots (FMKs) at two locations on the main shell and for three bright circumstellar knots (QSFs) near the southwest rim of Cas A. The main shell FMKs in Cas A exhibit a sparse near-infrared spectrum dominated by [S II] $1.03 \mu\text{m}$ emission with a handful of other, fainter emission lines. Among these are two high-ionization silicon lines, [Si VI] $1.96 \mu\text{m}$ and [Si X] $1.43 \mu\text{m}$, which have been detected in AGNs and novae but never before in a supernova remnant. The near-infrared spectra of circumstellar QSFs in Cas A show a much richer spectrum, with strong He I $1.083 \mu\text{m}$ emission and over a dozen bright [Fe II] lines. Observed [Fe II] line ratios indicate electron densities of $5 - 9 \times 10^4 \text{ cm}^{-3}$ in the QSFs. The Cas A QSF data are quite similar to the observed spectrum of a bright circumstellar knot along the northwest rim of the Kepler SNR, which also shows strong He I and [Fe II] emission with a measured electron density of $2.5 - 3 \times 10^4 \text{ cm}^{-3}$. Finally, we present *J*- and *K*-band images of Cas A. The *K*-band image shows faint diffuse emission which has no optical or mid-infrared counterpart but is morphologically similar to radio continuum maps and may be infrared synchrotron radiation.

Subject headings: supernova remnants — ISM: individual (Cassiopeia A, Kepler SNR) — ISM: lines and bands — circumstellar matter — infrared radiation

1. Introduction

The numerous optical and UV spectroscopic studies of supernova remnants (SNRs) in the literature have resulted in a rich catalog of observed emission-line features (cf. Fesen & Hurford 1996 and references therein). However, most of these studies do not extend much beyond 8500 \AA due to the poor sensitivity of optical detectors farther to the red. Only a handful of published SNR spectra go out as far as $1.1 \mu\text{m}$ where the most commonly seen features are [S III] $9069, 9532 \text{ \AA}$, [C I] $9823, 9850 \text{ \AA}$, [S II] $10287\text{--}10372 \text{ \AA}$, and He I 10830 \AA (e.g., Dennefeld & Andrillat 1981; Dennefeld 1982; Henry, MacAlpine, & Kirshner 1984).

With the maturing of high quantum efficiency near-infrared (NIR) detectors, it is now possible to probe the spectra of SNRs in the $1 - 5 \mu\text{m}$ wavelength regime, and there are a number of reasons

to do so. Near-infrared spectroscopy can provide access to features that aren't available in optical and UV spectra, such as molecular species like H_2 and CO, which can provide valuable information about molecule formation and destruction in SNRs. Molecular emission can also often be used as an astrophysical probe, providing information about temperature, density, and excitation mechanisms. In addition, there are many strong lines of [Fe II] in the NIR, which can be used as density diagnostics. These lines have higher critical densities than optical density sensitive lines, and thus can probe much higher densities ($\sim 10^3 - 10^5 \text{ cm}^{-3}$). Finally, the near-infrared contains several strong high-ionization species which have been seen in other objects like AGNs, novae, and planetary nebulae. These lines could provide important information about ionization processes and struc-

tures in supernova remnants.

Unfortunately, few NIR spectra of supernova remnants currently exist in the literature. Furthermore, there are almost no near-infrared data that take advantage of large-format array detectors allowing for spatially resolved long-slit spectroscopy and broad wavelength coverage. Indeed, of the few datasets available, most were obtained with relatively large apertures ($\sim 5'' - 20''$) in narrow wavelength regions typically covering only a single emission feature with each bandpass.

To date, the most comprehensive work on the NIR spectra of supernova remnants has been the study of molecular hydrogen (H_2) emission from shocks running into molecular clouds. This has been seen in IC 443, RCW 103, and the Cygnus Loop (Treffers 1979; Graham, Wright, & Longmore 1987; Oliva, Moorwood, & Danziger 1989, 1990; Burton & Spiromilio 1993; Graham et al. 1991; Graham, Wright, & Geballe 1991; Richter, Graham, & Wright 1995). H_2 has also been detected in the Crab Nebula (Graham, Wright, & Longmore 1990), presumably from dense, neutral cores of the emission-line filaments.

Other near-infrared work on SNRs has focused on [Fe II] line emission, which is typically two orders of magnitude brighter, relative to H I, than that seen in H II regions (Seward et al. 1983; Oliva, Moorwood, & Danziger 1989, hereafter OMD89). The large [Fe II]/H I ratios observed have been suggested as a good tracer for shocks in extragalactic studies (e.g., OMD89), and near-infrared [Fe II] imaging has been used to probe extragalactic SNR populations (e.g. Greenhouse et al. 1997). However, a large [Fe II]/H I ratio is not always an indication of shocks as the strong [Fe II] emission seen in the Crab Nebula is likely a result of photoionization (Graham, Wright, & Longmore 1990). Also, relative NIR [Fe II] line ratios have been used to deduce electron densities for Kepler, N63A, N49, N103B (OMD89), RCW 103 (OMD89; Oliva, Moorwood, & Danziger 1990, hereafter OMD90), and the Crab Nebula (Rudy, Rossano, & Puetter 1994).

In this paper, we present 0.95 – 2.4 μm spectra of shocked, metal-rich ejecta in the Cassiopeia A (Cas A) supernova remnant as well as J - and K -band images. To our knowledge, these are the first published NIR spectra of a young, “oxygen-rich” supernova remnant. We also present NIR spectra

of shocked circumstellar mass-loss material, both in Cas A and in Kepler’s SNR.

2. Observations and Data Reduction

Low-dispersion near-infrared spectroscopy and imaging of the Cas A and Kepler supernova remnants were obtained with the 2.4m Hiltner telescope at MDM Observatory on the southwest ridge of Kitt Peak in Arizona. Spectroscopic observations of Cas A took place in late November and early December 1999. J - and K -band images of Cas A were obtained in November 2000. Kepler’s SNR was observed in April 2000.

All observations were obtained with TIFKAM (a.k.a. ONIS), a high-throughput infrared imager and spectrograph with an ALLADIN 512×1024 InSb detector. This instrument can be operated with standard J , H , and K filters for broadband imaging, or with a variety of grisms, blocking filters, and an east-west oriented $0''.6$ slit, allowing low ($R \approx 700$) and moderate ($R \approx 1400$) resolution spectroscopic observations from 0.95 to 2.5 μm .

J - and K -band imaging of Cas A was performed using the following procedure: Sets of four dithered 30 s on-target images were immediately followed by four dithered 30 s images of fields $\approx 10'$ off-target. The off-target images were averaged together with high-pixel rejection to remove stars, creating sky background images which were then subtracted from the on-target images. This process was repeated four times for each on-target pointing. The entire remnant was covered in several overlapping positions resulting in total on-target integration times of 32 – 64 minutes in K -band, and 24 – 48 minutes in J -band. Sky-subtracted on-target images were registered and combined using standard IRAF tasks. J -band imaging of the Kepler SNR was performed in a similar manner, but with only one on-target position and 8 minutes total on-target integration time.

Near-infrared 0.95 – 2.4 μm long-slit spectra of Cas A and Kepler were obtained using three spectroscopic setups covering the 0.95 – 1.8 μm , 1.2 – 2.2 μm , and 2.0 – 2.4 μm wavelength regions. In Cas A, five metal-rich ejecta knots (FMKs: “Fast-Moving Knots”) were observed at two slit positions on the main shell and three

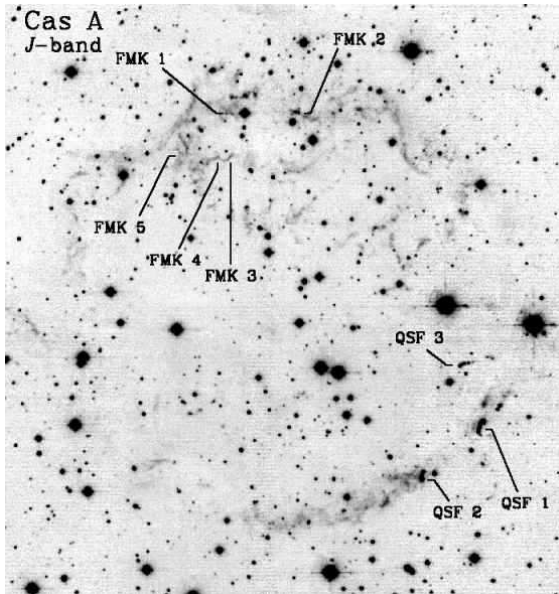


Fig. 1.— *J*-band image of Cas A with the locations of the observed FMKs and QSFs marked. North is up and East is to the left.

bright knots of circumstellar mass-loss material (QSFs: “Quasi-Stationary Flocculi”) were observed near the southwest rim of the remnant. The Kepler SNR was observed at a single position on the northwest rim, the region with the brightest optical emission. The spectroscopically observed regions of Cas A and Kepler are marked on the *J*-band images shown in Figures 1 and 2.

Table 1 lists the log of spectroscopic exposures for each slit position. Between on-target exposures the telescope was dithered along the slit to sample the array at multiple locations. For sufficiently isolated knots (QSF 1, QSF 3 and Kepler), dithered on-target exposures were used for first-order night-sky subtraction. For the other regions (QSF 2 and the FMKs), night-sky spectra were obtained between on-target exposures by observing an empty location 10′ north of the remnant and then removed from the on-target data. Figures 3 and 4 show representative 2-D long-slit spectra of FMKs 1 & 2 and QSF 1 in Cas A. Each frame shown is a single 900 s exposure in a single spectroscopic setup after first-order night-sky subtraction has been performed. 1-D spectra were extracted from these 2-D frames using standard IRAF tasks.

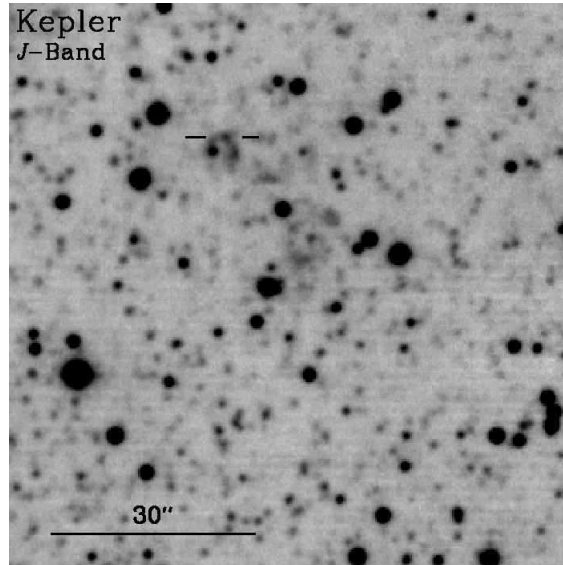


Fig. 2.— *J*-band image of Kepler with the location of the observed circumstellar knot marked. North is up and East is to the left.

Arc-lamps were observed at each telescope position to provide wavelength calibration.

The spectra were corrected for telluric absorption by observing nearby A stars and early G dwarfs from the Bright Star Catalog (Hoffleit & Jaschek 1982). Applying the procedure described by Hanson, Rieke, & Luhman (1998, hereafter HRL98), stellar features were removed from the G dwarf spectra by dividing by a normalized solar spectrum (Livingston & Wallace 1991; Wallace, Hinkle, & Livingston 1993)¹. The resulting spectra were used to correct for telluric absorption in the A stars. The hydrogen features in the corrected A star spectra were removed from the raw A star spectra and the results were used to correct the target data for telluric absorption. [For further discussion of this procedure see HRL98; Hanson, Conti, & Rieke (1996), and references therein.] The instrumental response was calibrated by matching the continuum of the A star telluric standards to the stellar atmosphere models of Kurucz (1994).

After correction for instrumental response and

¹NSO/Kitt Peak FTS data used here were produced by NSF/NOAO.

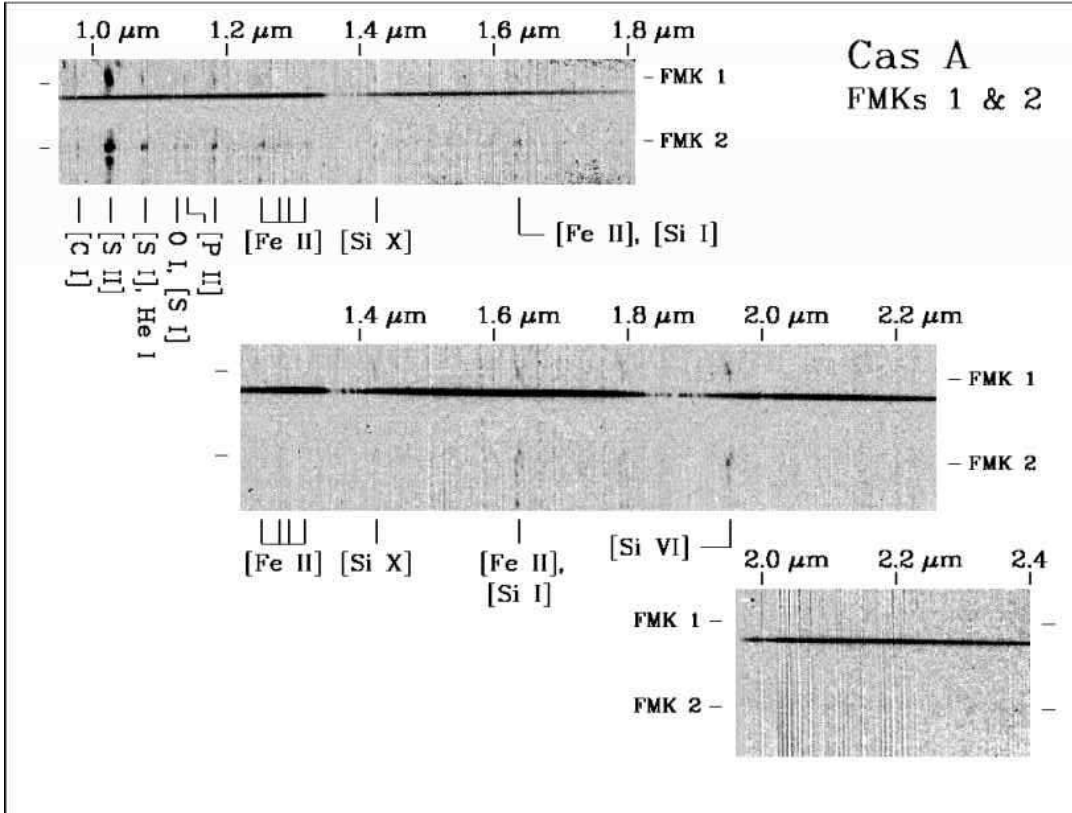


Fig. 3.— 2-D long-slit spectra of Cas A FMKs 1 & 2. Each frame shows a single 900 s exposure from a spectroscopic setup. Full 0.95–2.4 μm coverage was achieved with three overlapping spectroscopic setups. First order removal of night-sky lines has been performed, but the data shown are not corrected for telluric absorption or instrumental response. The approximate wavelength scale (in μm) is marked along the top of each frame, and the positions of the various observed features are shown at the bottom. Lines at the left and right of each frame denote the ends of the 1-D extraction apertures.

telluric absorption, the data for each knot in given spectroscopic setup were averaged together. Data taken with different setups were then flux-matched in the overlapping wavelength regions, and joined together to make a single, full coverage 1-D spectrum. Three Massey & Gronwall (1990) spectrophotometric standards were observed to set the absolute flux levels. The resulting absolute flux calibration is believed accurate to $\simeq 20\%$ shortward of 1.8 μm , and $\simeq 30\%$ from 1.8 to 2.4 μm .

3. Results & Discussion

Observed spectra of FMK 1 and QSF 1 in Cas A are presented in Figures 5 and 6 respectively with the spectrum of the west rim of the

Kepler SNR shown in Figure 7. Line identifications for the Cas A FMK spectra are presented in Table 2 (FMKs 1 & 2) and Table 3 (FMKs 3, 4 & 5) along with measured line centers and line fluxes, both observed and dereddened. Table 4 shows the line identifications and observed and dereddened fluxes for the Cas A QSFs and the western knot in Kepler. All wavelengths are given as vacuum values. Dereddening of the observed spectra was performed using the extinction curve of Cardelli, Clayton, & Mathis (1989). For the Cas A data, $E(B-V) = 1.5$ was used although the actual extinction varies significantly across the remnant (Hurford & Fesen 1996, hereafter HF96). For the Kepler data, we assumed $E(B-V) = 0.9$ (Blair, Long, & Vancura 1991)

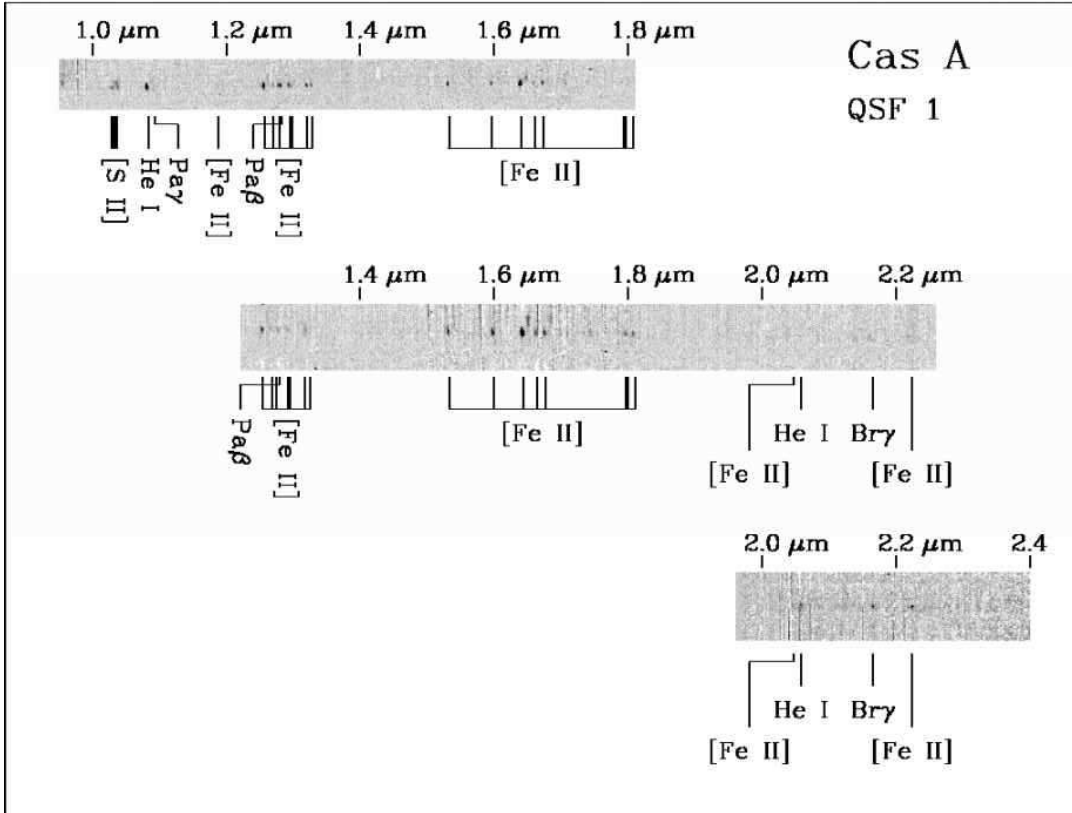


Fig. 4.— 2-D long-slit spectra of QSF 1 in Cas A. Each frame shows a single 900 s exposure from a spectroscopic setup. Full 0.95–2.4 μm coverage was achieved with three overlapping spectroscopic setups. First order removal of night-sky lines has been performed, but the data shown are not corrected for telluric absorption or instrumental response. The approximate wavelength scale (in μm) is marked along the top of each frame, and the positions of the various observed features are shown at the bottom. [S II] and [Fe II] emission from a faint FMK can be seen just above the QSF spectrum.

3.1. Cas A FMK Spectra

Optical spectra of Cas A ejecta knots (FMKs) exhibit strong forbidden oxygen and sulfur emission, and contain a number of fainter metal lines. These spectra show no indication of H or He, and little, if any, [Fe II] emission (HF96). (Note: Complete 4000 – 10500 \AA optical spectra of FMKs 1 and 2 are presented by HF96.) The near-infrared spectra of Cas A FMKs are intrinsically faint compared to their optical emission, and they are dominated by the [S II] 1.03 μm blend. A handful of other faint, low-ionization forbidden lines are seen including [C I] 0.9827 μm , 0.9853 μm , [P II] 1.1471 μm , 1.1886 μm , and [Fe II] 1.2570 μm , 1.6440 μm . We note that the 1.6440 μm feature

could be blended with [Si I] 1.646 μm emission. In FMK 2, the brightest FMK we observed in Cas A, three other faint [Fe II] lines (1.2791 μm , 1.2946 μm , & 1.3209 μm) were weakly detected. Two other weak lines near 1.08 μm and 1.13 μm could be emission from the [S I] $^3\text{P}^{-1}\text{D}$ doublet, but could also be due to (or blended with) He I 1.083 μm and O I 1.129 μm . O I emission would be consistent with the presence of weak permitted O I lines seen in the optical spectra of Cas A FMKs (e.g. HF96).

Perhaps the most interesting near-infrared lines detected in the brighter FMKs (1, 2, & 4) are those near the rest wavelengths of 1.43 μm and 1.96 μm . We identify these as high-ionization lines of silicon, [Si VI] 1.965 μm and [Si X] 1.4305 μm . The

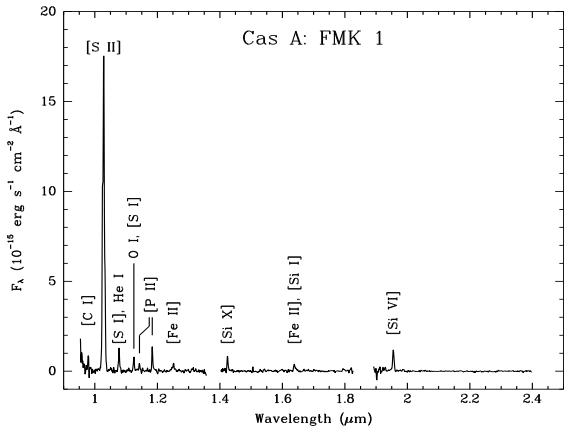


Fig. 5.— Observed NIR spectrum of FMK 1 in Cas A. The spectrum is dominated by strong [S II] emission, but also exhibits a number of other faint lines including [C I], [P II], [Fe II], and high-ionization lines of [Si VI] and [Si X].

detection of such high ionization species was unexpected as no other high-ionization lines are observed in optical or near-infrared spectra of Cas A. However, we could find no other likely line identifications that fit the observed wavelengths. There are weak H_2 transitions at wavelengths near both lines, but we find no evidence of emission present from the much stronger H_2 feature at $2.12 \mu\text{m}$. Also, the observed Doppler shifts of these lines, if identified as [Si VI] and [Si X], are consistent with each other and match those of the other lines seen in the FMKs to within the resolution of our data ($\approx 450 \text{ km s}^{-1}$). The absence of these lines in the spectra of the fainter FMKs is not significant as both of these lines suffer moderate telluric absorption and they could be too weak to detect in these fainter knots.

This is the first detection of these high-ionization silicon features in the spectrum of a supernova remnant. OMD90 looked for, but did not detect [Si VI] in their spectra of RCW 103. However, the [Si VI] $1.965 \mu\text{m}$ line has been seen in planetary nebulae (Ashley & Hyland 1988), and both the [Si VI] $1.965 \mu\text{m}$ and [Si X] $1.4305 \mu\text{m}$ lines have been reported in NIR spectra of the solar corona (Münch, Neugebauer, & McCammon 1967), novae (Benjamin & Dinerstein 1990; Green-

house et al. 1990), and AGNs (Oliva & Moorwood 1990; Thompson 1996; Murphy et al. 2000). Another high-ionization silicon line, [Si VII] $2.48 \mu\text{m}$, has also been observed in many of these objects, but this line was outside the observed bandpass of the Cas A spectra shown here. However, in follow-up observations made in November 2000 this line was detected in $1.4 - 2.5 \mu\text{m}$ spectra of FMKs 1 & 2.

NIR spectra of novae often show other strong high-ionization features such as [S IX] $1.252 \mu\text{m}$, [S IX] $1.392 \mu\text{m}$, [Cr XI] $1.550 \mu\text{m}$, [P VIII] $1.736 \mu\text{m}$, [Al IX] $2.040 \mu\text{m}$, and [Ca VIII] $2.323 \mu\text{m}$ (Wagner & DePoy 1996), none of which are seen in our Cas A data. (Note: [S IX] $1.252 \mu\text{m}$ would be blended with [Fe II] $1.257 \mu\text{m}$, and [S IX] $1.392 \mu\text{m}$ is obscured by strong telluric absorption). On the other hand, in near-infrared AGN spectra the [Si VI], [Si VII], and [Si X] lines are often the only strong high-ionization features seen in the $0.95 - 2.5 \mu\text{m}$ region.

Near-infrared “coronal” line emission in novae, AGNs, and planetary nebulae is believed to be due to photoionization, although collisional ionization from hot, shocked gas often cannot be ruled out. In contrast, the low-ionization optical spectra of Cas A’s FMK knots have been modelled as shocks with a photoionized precursor component (Sutherland & Dopita 1995; HF96). Observed ratios of lines at different ionization levels are explained in these models as a mixture of emission from the rapidly cooling post-shock region, and from a precursor in the ejecta out ahead of the reverse-shock which is photoionized by UV emission from the shock front. Unfortunately, no predictions for [Si VI] and [Si X] emission have been made so it is unclear if the shock/precursor models can explain these very high ionization lines. Alternatively, the high-ionization emission might be understood with a pure photoionization model like those used to explain the high-ionization lines seen in novae, AGNs and planetary nebulae. The main shell of Cas A is quite bright in X-rays (Hughes et al. 2000; Hwang, Holt, & Petre 2000) which could provide a strong photoionizing source.

In any case, it also seems likely that abundances play some role in the detection of these high-ionization silicon lines. Spectral modeling of optical FMK spectra indicate significant enrichment of metal abundances, suggesting that FMKs

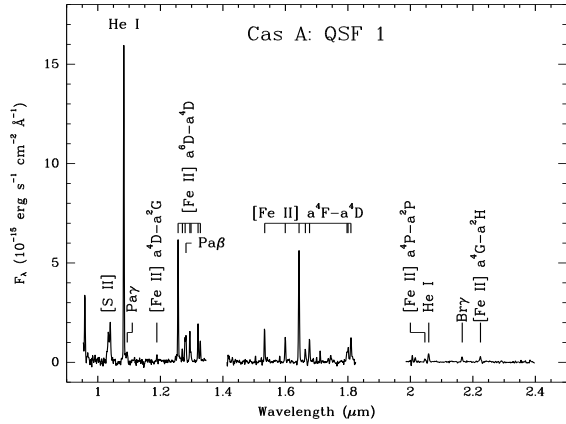


Fig. 6.— Observed NIR spectrum of QSF 1 in Cas A. The spectrum is dominated by strong He I 1.083 μm and [Fe II] emission lines.

are gas from the inner regions of the exploded star (Chevalier & Kirshner 1979, HF96). Furthermore, X-ray imaging of Cas A has detected bright silicon line emission from the main shell ejecta (Hwang, Holt, & Petre 2000). All of this indicates that the FMKs are likely silicon-rich and so it may be that only a small fraction of the silicon is highly ionized with the bulk of the gas in a much lower ionization state. However, without a detailed spectral model it is impossible to conclude that the detection of these silicon lines is merely an abundance effect as these lines are also detected in AGNs and planetary nebulae where the silicon abundance is much lower. In fact, with respect to the observed high-ionization lines, the Cas A spectra more closely resemble near-infrared AGN spectra than NIR spectra of novae, even though the gas in novae is probably closer in composition to the FMKs.

3.2. Cas A QSFs and Kepler

The optical spectra of shocked circumstellar knots in Cas A (QSFs) and Kepler’s SNR are dominated by strong [N II] emission, with only a few other weak lines of H and He. These knots are thought to be nitrogen enriched material shed by the progenitor star prior to the explosion, and then shocked by the expanding blast wave (Peimbert & van den Bergh 1971). The NIR spectra of these knots seem consistent with this picture, exhibit-

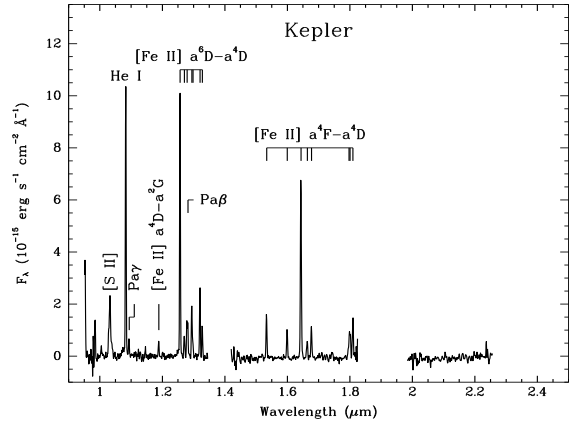


Fig. 7.— Observed NIR spectrum of a bright circumstellar knot on the west rim of Kepler’s SNR. The spectrum is dominated by strong He I 1.083 μm and [Fe II] emission lines.

ing an ISM-like spectrum with the strong [Fe II] emission typical of shocked gas. The Cas A QSFs and the Kepler knot are relatively bright in the near-infrared, especially in the *J* ($\sim 1.2 \mu\text{m}$) and *H* ($\sim 1.6 \mu\text{m}$) bands due to this rich [Fe II] spectrum. In addition to the [Fe II] lines, these circumstellar knots also show strong He I 1.083 μm emission, as well as the [S II] 1.03 μm blend, [C I] 0.9827 μm , 0.9853 μm , He I 2.058 μm , and faint hydrogen lines (Pa γ 1.0941 μm , Pa β 1.2822 μm , and Br γ 2.1661 μm). In fact, our QSF and Kepler spectra resemble the 1.4–2.4 μm spectrum of the optically brightest region of RCW 103 presented by OMD90 except that no H₂ emission was seen.

Several of the observed [Fe II] line ratios can be used as density diagnostics (e.g. Nussbaumer & Storey 1980; OMD89; OMD90). Using the dereddened ratios of the 1.5339 μm , 1.5999 μm , and 1.6642 μm lines to the strong 1.6440 μm line and the predicted ratios of OMD90, we estimated electron densities for each of the three QSFs in Cas A and for the Kepler knot. The results are shown in Table 5. In each case, the various line ratios all gave mutually consistent estimates of the electron density for a given knot. The dereddened line ratios in each of the three QSFs observed in Cas A are indistinguishable to within the measurement errors and yield electron densities of 5

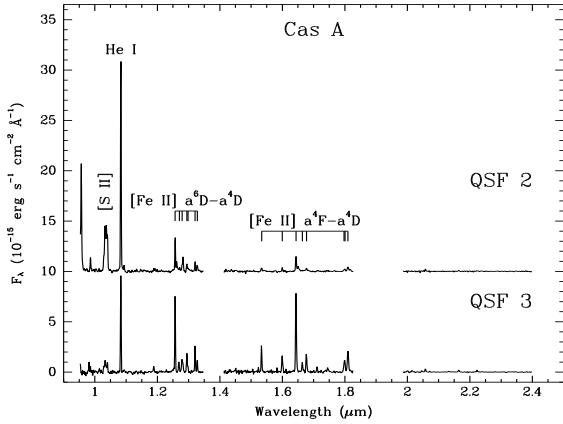


Fig. 8.— Observed NIR spectrum of QSF 2 and QSF 3 in Cas A, showing the large variation of the He I/[Fe II] emission ratio seen in the Cas A QSF data. The QSF 2 data have been shifted vertically by 10 units for clarity.

$-9 \times 10^4 \text{ cm}^{-3}$, which approach the high-density limit of the [Fe II] lines.

The density of the Kepler knot is roughly half that measured in the Cas A QSFs, namely $2.5 - 3.1 \times 10^4 \text{ cm}^{-3}$. Our estimate for the density of Kepler is somewhat higher than that measured at roughly the same position by OMD89, although it might be consistent with their upper limit. Differences in density estimates are not unexpected as OMD89 used a larger aperture ($5''.8 \times 5''.9$ vs. our $0''.6$ slit) and therefore sampled a much larger region of the remnant's northwest emission filaments.

Although electron densities in the three observed Cas A QSFs are similar, the He I to [Fe II] emission ratio varies dramatically. This is seen in Figure 8 which shows the observed NIR spectra of QSF 2 and QSF 3. In QSF 2, the He I $1.083 \mu\text{m}$ line is much brighter than the brightest [Fe II] lines, while in QSF 3, these lines are of nearly equal strength. Table 5 lists the dereddened He I $1.083 \mu\text{m}$ to [Fe II] $1.257 \mu\text{m}$ line ratio which varies by nearly a factor of five in the three QSFs observed in Cas A. The observed variation could be due to temperature effects or compositional differences in the knots, for instance, in the depletion of gaseous iron into dust grains.

3.3. *J*- and *K*-band images of Cas A

J- and *K*-band mosaic images of Cas A are presented in Figures 9 and 10 respectively. In both images, the brightest emission comes from the QSFs. In *J*-band, this emission is almost entirely due to strong [Fe II] lines, while the *K*-band emission is a mixture of [Fe II], He I, and Br γ . The relative brightness of the QSFs in the two bands (i.e. the *J* – *K* color) changes from knot to knot, and the NIR luminosity is poorly correlated with the optical luminosity. This may be related to the large variation of the observed He I $1.083 \mu\text{m}$ to [Fe II] $1.257 \mu\text{m}$ line ratio seen in the NIR spectra of the QSFs.

The FMK ejecta knots are also clearly visible in the *J*-band image. In this case, the emission is a mixture of weak [Fe II] and [P II] emission lines. Some FMK filaments are also visible in the *K*-band image, particularly in the inner regions of the remnant. The spectra of the bright northern FMKs showed no emission in *K*-band, but the [Si VI] $1.96 \mu\text{m}$ line lies at the blue edge of the *K*-band filter. Thus the *K*-band filter may be picking up [Si VI] emission from filaments with large positive radial velocities. This is supported by the fact that the filamentary emission in *K*-band largely disappears near the rim of Cas A, and is seen primarily in the inner regions of the remnant where the radial velocities are largest.

The dominant feature in the *K*-band image is diffuse emission which forms a nearly complete ring around the rim of Cas A and also fills some of the interior. This diffuse emission can be faintly seen in the *J*-band image near the center and at several positions on the rim. This diffuse emission has no optical counterpart and does not correspond well to X-ray or mid-IR images of Cas A either (cf. HF96; Lagage et al. 1996), but it does exhibit morphological similarities to radio continuum images (e.g. Anderson & Rudnick 1995). Some hint of the morphological differences between *K*-band and optical images has been seen in the 2MASS images of Cas A (Van Dyk 1999).

The lack of any detected diffuse line emission in the 2-D spectra of FMKs and QSFs on the rim (specifically FMKs 1 & 2, and QSFs 1 & 2) suggest that the diffuse emission is continuum rather than line emission. The large morphological differences between the *K*-band and mid-IR images, and the

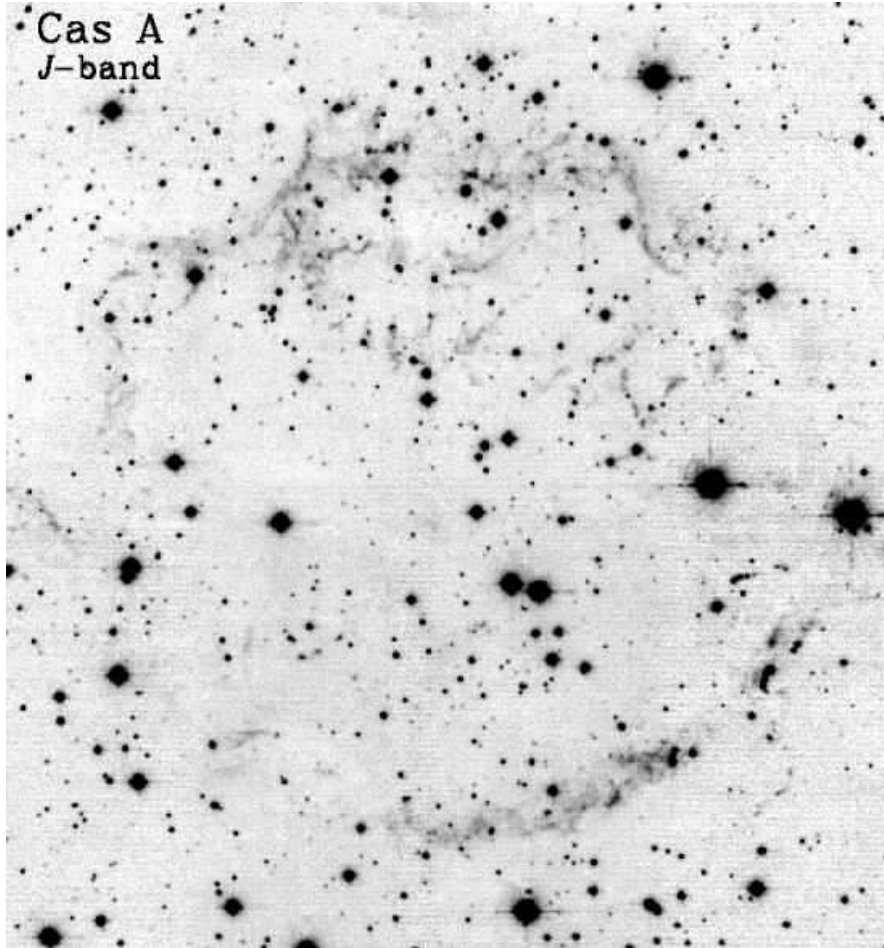


Fig. 9.— *J*-band image of Cas A. North is up and East is to the left. The *J*-band image is similar to optical images of Cas A with both circumstellar knots (QSFs) and ejecta knots (FMKs) clearly visible. Diffuse emission is also faintly detected in the *J*-band near the center of the remnant and around the rim to the north and west.

detection of the diffuse emission in *J*-band argue against thermal dust emission as a source. The thermal dust emission seen in the mid-infrared is well correlated to the optical knots (Lagage et al. 1996), and the detection of thermal emission in *J*-band would probably require prohibitively high dust temperatures at or above typical grain destruction limits. On the other hand, the morphological similarity of the diffuse emission with radio continuum images suggests that the diffuse *K*-band emission may be infrared synchrotron radiation.

4. Conclusion

We have presented the first near-infrared (NIR) spectra of a young, metal-rich supernova remnant. The spectra of fast-moving ejecta knots in Cas A are dominated by [S II] $1.03 \mu\text{m}$ emission, but show several other faint emission lines including high-ionization lines of [Si VI] and [Si X]. These forbidden silicon lines have often been seen in NIR spectra of novae and AGNs but have never before been detected in a supernova remnant. Interestingly, the silicon lines represent a much higher ionization state than the observed optical and near-infrared emission lines. Therefore, further study of

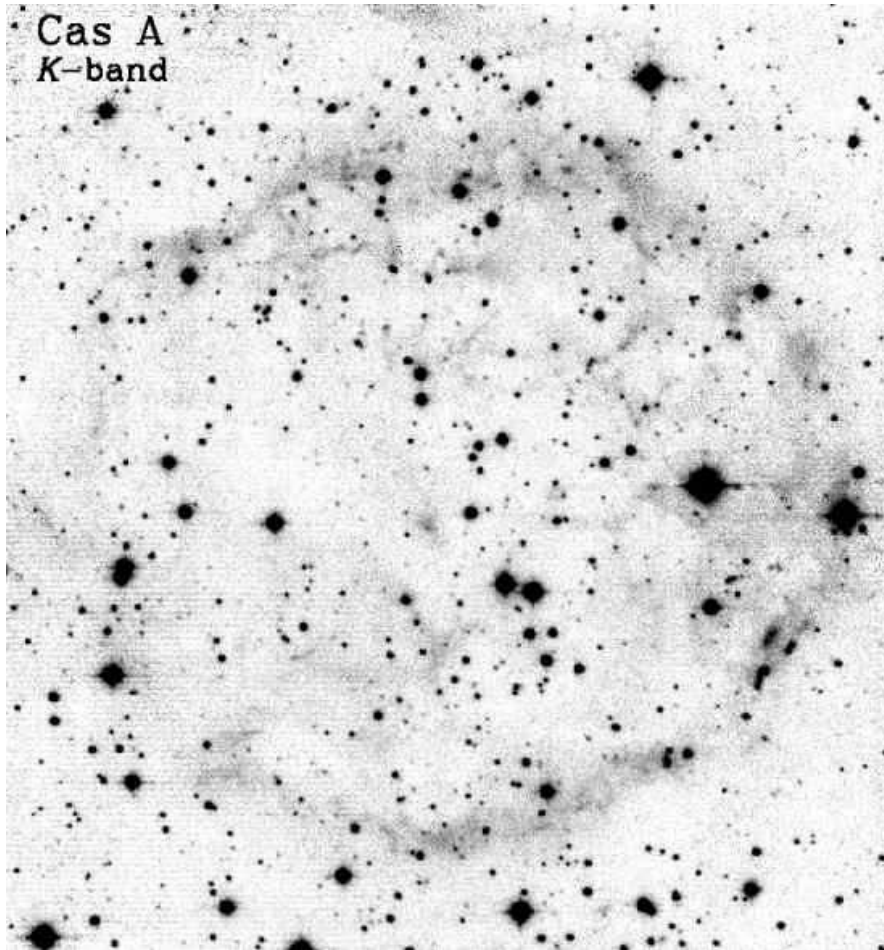


Fig. 10.— *K*-band image of Cas A. North is up and East is to the left. The dominant feature is diffuse emission that forms a nearly complete ring. The diffuse emission exhibits morphological similarities to radio continuum maps of Cas A.

the spatial distribution of the [Si VI] and [Si X] line emission may provide valuable information about the ionization structure in the metal-rich Cas A ejecta.

We also obtained NIR spectra of shocked circumstellar knots in Cas A and Kepler, which are shown to have bright He I and [Fe II] emission. Analysis of relative [Fe II] line ratios indicate electron densities $\sim 10^4 - 10^5 \text{ cm}^{-3}$ in these knots. While the measured density was relatively constant for the three circumstellar knots observed in Cas A, the He I/[Fe II] emission ratios were found to vary by nearly a factor of five.

Finally, we presented *J* and *K*-band images of

Cas A. While the *J*-band image is largely similar to optical images, the dominant feature in the *K*-band is diffuse emission that best matches radio continuum images of Cas A and may be near-infrared synchrotron emission.

We would like to thank Bob Barr and the MDM staff for their excellent assistance in instrument setup and general observing support. This research is supported by NSF Grant 98-76703.

REFERENCES

- Anderson M. C., & Rudnick L. 1995, *ApJ*, 441, 307
- Ashley, M. C. B., & Hyland, A. R. 1988, *ApJ*, 331, 532
- Benjamin, R. A., & Dinerstein, H. L. 1990, *AJ*, 100, 1588
- Blair, W. P., Long, K. S., & Vancura 1991, *ApJ*, 366, 484
- Burton, M., & Spyromilio, J. 1993, *PASAu*, 10, 327
- Cardelli, J. A., Clayton, G. C., & Mathis, J. S. 1989, *ApJ*, 345, 245
- Chevalier, R. A., & Kirshner, R. P. 1979, *ApJ*, 223, 154
- Dennefeld, M. 1980, *A&A*, 112, 215
- Dennefeld, M., & Andriolat, Y. 1981, *A&A*, 103, 44
- Fesen, R. A., & Hurford, A. P. 1996, *ApJS*, 106, 563
- Graham, J. R., Wright, G. S., & Longmore, A. J. 1987, *ApJ*, 313, 847
- Graham, J. R., Wright, G. S., & Longmore, A. J. 1990, *ApJ*, 352, 172
- Graham, J. R., Wright, G. S., & Geballe, T. R. 1991, *ApJ*, 372, 21
- Graham, J. R., Wright, G. S., Hester, J. J., & Longmore, A. J. 1991, *AJ*, 101, 175
- Greenhouse, M. A., Grasdalen, G. L., Woodward, C. E., Benson, J., Gehrz, R. D., Rosenthal, E., & Skrutskie, M. F. 1990, *ApJ*, 352, 307
- Greenhouse, M. A., Satyapal, S., Woodward, C. E., Fischer, J., Thompson, K. L., Forrest W. J., Pipher, J. L., Raines, N., Smith, H. A., Watson, D. M., & Rudy, R. J. 1997, *ApJ*, 476, 105
- Hanson, M. M., Conti, P. S., & Rieke, M. J. 1996, *ApJS*, 107, 281
- Hanson, M. M., Rieke, G. H., & Luhman, K. L. 1998, *AJ*, 116, 1915 (HRL98)
- Henry, R. B. C., MacAlpine, G. M., & Kirshner, R. P. 1984, *ApJ*, 278, 619
- Hoffleit, D., & Jaschek, C. 1982, *The Bright Star Catalog, 4th Revised Edition* (New Haven: Yale University Observatory)
- Hughes, J. P., Rakowski, C. E., Burrows, D. N., & Slane, P. O. 2000, *ApJ*, 528, 109
- Hurford, A. P., & Fesen, R. A. 1996 *ApJ*, 469, 246 (HF96)
- Hwang, U., Holt, S. S., & Petre, R. 2000, *ApJ*, 537, 119
- Kurucz, R. L. 1994, *Solar Abundance Model Atmospheres for 0,1,2,4,8 km/s*, Kurucz CD-Rom No. 19
- Lagage P. O., Claret A., Ballet J., Boulanger F., Cesarsky C. J., Cesarsky D., Fransson C., & Pollock A. 1996, *A&A*, 315, 273
- Livingston, W., & Wallace, L. 1991 July, NSO Tech. Rept. #91-001
- Massey, P., & Gronwall, C. 1990, *ApJ*, 358, 344
- Münch, G., Neugebauer, G., & McCammon, D. 1967, *ApJ*, 149, 681
- Murphy, T. W. Jr., Soifer, B. T., Matthews, K., & Armus, L. 2000, *AJ*, 120, 1675
- Nussbaumer, H., & Storey, P. J. 1980, *A&A*, 89, 308
- Oliva, E., Moorwood, A. F. M., & Danziger, I. J. 1989, *A&A*, 214, 307 (OMD89)
- 1990, *A&A*, 240, 453 (OMD90)
- Oliva, E. & Moorwood, A. F. M. 1990, *ApJ*, 348, 5
- Peimbert M., & van den Bergh, S. 1971, *ApJ*, 167, 223
- Richter, M. J., Graham, J. R., & Wright, G. S. 1995, *ApJ*, 454, 227
- Rudy, R. J., Rossano, G. S., & Puetter, R. C. 1994, *ApJ*, 426, 646
- Seward, F. D., Harnden, F. R. Jr., Murdin, P., & Clark, D. H. 1983, *ApJ*, 267, 698

Sutherland, R. S., & Dopita, M. A. 1995, ApJ,
439, 381

Thompson, R. I. 1996 ApJ, 459, 61

Treffers, R. R. 1979, ApJ, 223, L17

Van Dyk, S. 1999,
<http://www.ipac.caltech.edu/2mass/gallery/powarc8.html>

Wallace, L., Hinkle, K., & Livingston, W., 1993
April, NSO Tech. Rept. #93-001

Wagner, R. M., & DePoy, D. L. 1996, ApJ, 467,
860

TABLE 1
LOG OF OBSERVATIONS

Slit Position	Bandpass (μm)	Exposure (s)
FMK 1 & 2	0.95 – 1.8	7×900
	1.2 – 2.2	3×900
	2.0 – 2.4	2×900
FMK 3, 4 & 5	0.95 – 1.8	6×900
	1.2 – 2.2	3×900
QSF 1	0.95 – 1.8	5×900
	1.2 – 2.2	3×900
	2.0 – 2.4	6×900
QSF 2	0.95 – 1.8	3×900
	1.2 – 2.2	7×900
	2.0 – 2.4	3×900
QSF3	0.95 – 1.8	3×900
	1.2 – 2.2	3×900
	2.0 – 2.4	3×900
Kepler	0.95 – 1.8	10×900
	1.2 – 2.2	5×900

TABLE 2
LINE IDENTIFICATIONS FOR FMKS 1 & 2

λ_{lab} (μm)	Line ID	FMK 1			FMK 2		
		$\lambda_{\text{obs}}(\mu\text{m})$	I(λ)	F(λ) ^a	$\lambda_{\text{obs}}(\mu\text{m})$	I(λ)	F(λ) ^a
0.9827, 0.9853	[C I] $^3\text{P}_{1,2}^{-1}\text{D}_2$	0.979	31	253	0.981	58	349
1.0290, 1.0323, 1.0339, 1.0373	[S II] $^2\text{D}_{5/2,3/2}^{-2}\text{P}_{3/2,1/2}$	1.028	1280	6650	1.027	3090	11600
1.0824	[S I] $^3\text{P}_2^{-1}\text{D}_2$	1.078	54	250	1.079	228	1043
1.0832	He I $^3\text{S}_1^{-3}\text{P}_{0,1,2}$						
1.1289, 1.1290	O I $^3\text{P}_{0,1,2}^{-3}\text{D}_{1,2,3}$	1.125	33	139	1.125	55	238
1.1309	[S I] $^3\text{P}_1^{-1}\text{D}_2$						
1.1471	[P II] $^3\text{P}_1^{-1}\text{D}_2$	1.143	20	79	1.142	39	160
1.1886	[P II] $^3\text{P}_2^{-1}\text{D}_2$	1.184	50	186	1.183	103	375
1.2570	[Fe II] $\text{a}^6\text{D}_{9/2}^{-\text{a}^4}\text{D}_{7/2}$	1.251	37	120	1.254	76	253
1.2791	[Fe II] $\text{a}^6\text{D}_{3/2}^{-\text{a}^4}\text{D}_{3/2}$	1.279	21	67
1.2946	[Fe II] $\text{a}^6\text{D}_{5/2}^{-\text{a}^4}\text{D}_{5/2}$	1.293	23	66
1.3209	[Fe II] $\text{a}^6\text{D}_{7/2}^{-\text{a}^4}\text{D}_{7/2}$	1.319	17	50
1.4305	[Si X] $^2\text{P}_{1/2}^{-2}\text{P}_{3/2}$	1.425	35	93	1.424	76	111
1.6440	[Fe II] $\text{a}^4\text{F}_{9/2}^{-\text{a}^4}\text{D}_{7/2}$	1.639	27	59	1.638	54	118
1.6459	[Si I] $^3\text{P}_2^{-1}\text{D}_2$						
1.965	[Si VI] $^2\text{P}_{3/2}^{-2}\text{P}_{2/2}$	1.955	69	124	1.952	268	480

NOTE.—Line fluxes in units of 10^{-15} erg s⁻¹ cm⁻²

^aCorrected for $E(B-V) = 1.5$

TABLE 3
LINE IDENTIFICATIONS FOR FMKS 3, 4, & 5

λ_{lab} (μm)	Line ID	FMK 3			FMK 4			FMK 5		
		$\lambda_{\text{obs}}(\mu\text{m})$	I(λ)	F(λ) ^a	$\lambda_{\text{obs}}(\mu\text{m})$	I(λ)	F(λ) ^a	$\lambda_{\text{obs}}(\mu\text{m})$	I(λ)	F(λ) ^a
0.9827, 0.9853	[C I] $^3\text{P}_{1,2}-^1\text{D}_2$	0.977	22	128	0.978	51	306
1.0290, 1.0323, 1.0339, 1.0373	[S II] $^2\text{D}_{5/2,3/2}-^2\text{P}_{3/2,1/2}$	1.025	464	2450	1.025	412	2210	1.044	156	784
1.0824	[S I] $^3\text{P}_2-^1\text{D}_2$	1.075	41	186	1.075	30	139	1.096	15	61
1.0832	He I $^3\text{S}_1-^3\text{P}_{0,1,2}$									
1.1289, 1.1290	O I $^3\text{P}_{0,1,2}-^3\text{D}_{1,2,3}$	1.122	31	135	1.122	25	106	1.144	6	24
1.1309	[S I] $^3\text{P}_1-^1\text{D}_2$									
1.1886	[P II] $^3\text{P}_2-^1\text{D}_2$	1.180	19	70	1.181	23	87	1.202	11	39
1.2570	[Fe II] $\text{a}^6\text{D}_{9/2}-\text{a}^4\text{D}_{7/2}$	1.248	16	57	1.248	16	60	1.271	20	64
1.4305	[Si X] $^2\text{P}_{1/2}-^2\text{P}_{3/2}$	1.420	16	40
1.6440	[Fe II] $\text{a}^4\text{F}_{9/2}-\text{a}^4\text{D}_{7/2}$	1.632	14	30	1.633	20	43	1.663	20	44
1.6459	[Si I] $^3\text{P}_2-^1\text{D}_2$									
1.965	[Si VI] $^2\text{P}_{3/2}-^2\text{P}_{2/2}$	1.951	20	36

NOTE.—Line fluxes in units of 10^{-15} erg s⁻¹ cm⁻²

^aCorrected for $E(B-V) = 1.5$

TABLE 4
LINE IDENTIFICATIONS FOR CAS A QSFs AND KEPLER SNR

λ_{rest} (μm)	Line ID	Cas A QSF 1		Cas A QSF 2		Cas A QSF 3		Kepler	
		I(λ)	F(λ) ^a	I(λ)	F(λ) ^a	I(λ)	F(λ) ^a	I(λ)	F(λ) ^b
0.9827, 0.9853	[C I] $^3\text{P}_{1,2}-^1\text{D}_2$	44	253	36	220	49	145
1.0290, 1.0323, 1.0339, 1.0373	[S II] $^2\text{D}_{5/2,3/2}-^2\text{P}_{3/2,1/2}$	111	595	(bl w/ FMK)		104	534	157	423
1.0832	He I $^3\text{S}_1-^3\text{P}_{0,1,2}$	450	2060	607	2780	276	1260	340	848
1.0941	H I Pa γ	16	71	14	65	9	37	17	42
1.1885	[Fe II] $\text{a}^4\text{D}_{7/2}-\text{a}^2\text{G}_{7/2}$	12	45	20	72	18	42
1.2570	[Fe II] $\text{a}^6\text{D}_{9/2}-\text{a}^4\text{D}_{7/2}$	173	572	95	315	211	700	329	675
1.2707	[Fe II] $\text{a}^6\text{D}_{1/2}-\text{a}^4\text{D}_{1/2}$	27	83	17	61	37	120	31	63
1.2791	[Fe II] $\text{a}^6\text{D}_{3/2}-\text{a}^4\text{D}_{3/2}$	85	269	65	210	78	250	79	160
1.2822	H I Pa β								
1.2946	[Fe II] $\text{a}^6\text{D}_{5/2}-\text{a}^4\text{D}_{5/2}$	60	185	39	118	70	218	82	162
1.2981	[Fe II] $\text{a}^6\text{D}_{1/2}-\text{a}^4\text{D}_{3/2}$								
1.3209	[Fe II] $\text{a}^6\text{D}_{7/2}-\text{a}^4\text{D}_{7/2}$	58	176	28	83	75	226	84	172
1.3281	[Fe II] $\text{a}^6\text{D}_{3/2}-\text{a}^4\text{D}_{5/2}$	32	97	28	87	36	107	35	72
1.5339	[Fe II] $\text{a}^4\text{F}_{9/2}-\text{a}^4\text{D}_{5/2}$	58	138	17	38	79	187	61	105
1.5999	[Fe II] $\text{a}^4\text{F}_{7/2}-\text{a}^4\text{D}_{3/2}$	46	104	12	27	67	151	44	71
1.6440	[Fe II] $\text{a}^4\text{F}_{9/2}-\text{a}^4\text{D}_{7/2}$	203	440	57	125	288	628	273	432
1.6642	[Fe II] $\text{a}^4\text{F}_{5/2}-\text{a}^4\text{D}_{1/2}$	28	61	39	80	29	45
1.6773	[Fe II] $\text{a}^4\text{F}_{7/2}-\text{a}^4\text{D}_{5/2}$	44	93	18	44	63	134	45	69
1.7976	[Fe II] $\text{a}^4\text{F}_{3/2}-\text{a}^4\text{D}_{3/2}$	54	108	14	27	68	134	70	99
1.8005	[Fe II] $\text{a}^4\text{F}_{5/2}-\text{a}^4\text{D}_{5/2}$								
1.8099	[Fe II] $\text{a}^4\text{F}_{7/2}-\text{a}^4\text{D}_{7/2}$	59	109	30	53	109	211	57	91
2.0466	[Fe II] $\text{a}^4\text{P}_{5/2}-\text{a}^2\text{P}_{3/2}$	9	16	7	12
2.0587	He I $^1\text{S}_0-^3\text{P}_1$	20	35	8	13	13	22
2.1661	H I Br γ	12	20	5	8	9	16
2.2244	[Fe II] $\text{a}^4\text{G}_{9/2}-\text{a}^2\text{H}_{11/2}$	15	23	5	8	8	12

NOTE.—Line fluxes in units of 10^{-15} erg s $^{-1}$ cm $^{-2}$.

^aCorrected for $E(B-V) = 1.5$

^bCorrected for $E(B-V) = 0.9$

TABLE 5
CAS A QSF & KEPLER: KNOT DENSITIES & HE I/[Fe II] FLUX RATIOS

Knot	$\frac{[\text{Fe II}] \lambda 1.5339}{[\text{Fe II}] \lambda 1.6440}$	$\frac{[\text{Fe II}] \lambda 1.5999}{[\text{Fe II}] \lambda 1.6440}$	$\frac{[\text{Fe II}] \lambda 1.6642}{[\text{Fe II}] \lambda 1.6440}$	n_e (10^4 cm^{-3})	$\frac{[\text{He I}] \lambda 1.0832}{[\text{Fe II}] \lambda 1.2570}$
Cas A QSF 1	0.314 ± 0.015	0.236 ± 0.015	0.139 ± 0.015	6.0 – 8.7	3.6 ± 0.2
Cas A QSF 2	0.304 ± 0.040	0.216 ± 0.040	...	3.2 – 8.9	8.8 ± 0.4
Cas A QSF 3	0.298 ± 0.010	0.240 ± 0.010	0.127 ± 0.010	5.2 – 6.9	1.8 ± 0.1
Kepler SNR	0.243 ± 0.015	0.164 ± 0.015	0.104 ± 0.015	2.5 – 3.1	1.3 ± 0.1